# Functional semi-automated segmentation of renal DCE-MRI sequences using a Growing Neural Gas algorithm

Chevaillier Beatrice[1], Collette Jean-Luc[1], Mandry Damien[2], Claudon Michel[2] & Pietquin Olivier[1,2]
*[1]SUPELEC-Metz campus, IMS Research Group*
*[2]IADI, INSERM, ERI 13 ; Nancy University*
*France*

## 1. Introduction

In this chapter we describe a semi-automatic segmentation method for dynamic contrast-enhanced magnetic resonance imaging (DCE-MRI) sequences for renal function assessment. Among the different MRI techniques aiming at studying the renal function, DCE-MRI with gadolinium chelates injection is the most widely used (Grenier et al., 2003). Several parameters like the glomerular filtration rate or the differential renal function can be non-invasively computed from perfusion curves of different Regions Of Interest (ROI). So segmentation of internal anatomical kidney structures like cortex, medulla and pelvo-caliceal cavities is crucial for functional assessment detection of diseases affecting different parts of this organ. Manual segmentation by a radiologist is fairly delicate because images are blurred and highly noisy. Moreover the different compartments are not visible during the same perfusion phase because of contrast changes: cavities are enhanced during late perfusion phase, whereas cortex and medulla can only be separated near the cortical peak, when the contrast agent enters the kidney (figure 1); consequently they cannot be delineated on a single image. Radiologists have to examine the whole sequence in order to choose the two most suitable frames: the operation is time-consuming and functional analysis can vary greatly in case of misregistration or through-plane motion. Some classical semi-automated methods are often used in the medical field but few of them have been tested on renal DCE-MRI sequences (Michoux et al., 2006). In (Coulam et al., 2002), cortex of pig kidneys is delineated by simple intensity thresholding during cortical enhancement phase, but precision is limited essentially because of noise. In (Lv et al., 2008), a three-dimensional kidney extraction and a segmentation of internal renal structures are performed using a region-growing technique. Anyway only few frames are used, so problems due frames selection and non corrected motion remain. As the contrast temporal evolution is different in every compartment for physiological reasons, pixels can be classified according to their time-intensity curves: such a method can improve both noise robustness and reproducibility. In (Zoellner et al., 2006), independent component analysis allows recovering

some functional regions but does not result in segmentations comparable to morphological ones: any pixel can actually be attributed to zero, one or more compartment. In (Sun et al., 2004), a multi-step approach including successive registrations and segmentations is proposed: pixels are classified using a K-means partitioning algorithm applied to their time-intensity curves. Nevertheless a functional segmentation using some unsupervised classification method and resulting in only three ROIs corresponding to cortex, medulla and cavities seems to be hard to obtained directly. This is mainly due to considerable contrast dissimilarities between pixels in a same compartment despite some common characteristics (Chevaillier et al., 2008a).

Concerning validation, very few results for real data have been exposed. In (Rusinek et al., 2007), a segmentation error is defined in connection with a manual segmentation as the global volume of false-positive (oversegmented) and false-negative (undersegmented) voxels. Nevertheless assessment consists mostly in qualitative consistency with manual segmentations or in comparisons between the corresponding compartment volumes or between the induced renograms (Song et al., 2005).

We propose to test a semi-automated split (2.1) and merge method (2.2) for renal functional segmentation. The kidney pixels are first clustered according to their contrast evolution using a vector quantization algorithm. These clusters are then merged thanks to some characteristic criteria of their prototype functional curves to get the three final anatomical compartments. Operator intervention consists only in a coarse tuning of two independent thresholds for merging, and is thus easy and quick to perform while keeping the practitioner into the loop. The method is also relatively robust because the whole sequence is used instead of only two frames as for traditional manual segmentation. In the absence of ground truth for results assessment, a manual anatomical segmentation by a radiologist is considered as a reference. Some discrepancy criteria are computed between this segmentation and functional ones. As a comparison, the same criteria are evaluated between the reference and another manual segmentation.

This book chapter is an extended version of (Chevaillier et al., 2008b).

## 2. Method for functional segmentation

### 2.1 Vector quantization of time-intensity curves

The temporal evolution of contrast for each of the $N$ pixels of a kidney results from a DCE-MRI registered sequence: examples of three frames for different perfusion phases can be seen in figure 1.

Let $I_{ip}$ be the intensity at time $p$ for the pixel $x_i$, $I_B$ the mean value for baseline and $I_L$ the mean value during late phase for the time-intensity curve of entire kidney. Let $\xi_i = \left(\xi_{i1},...,\xi_{iN_T}\right)$ be the $N_T$-components vector associated with each pixel, where $\xi_{ip} = \left(I_{ip} - I_B\right)/\left(I_L - I_B\right)$ (intensity normalization is performed in order to have similar dynamic for any kidney). The $N$ vectors $\xi_i$ are considered as samples of an unknown probability distribution over a manifold $X \subseteq R^{N_T}$ with a density of probability $p(\xi)$.
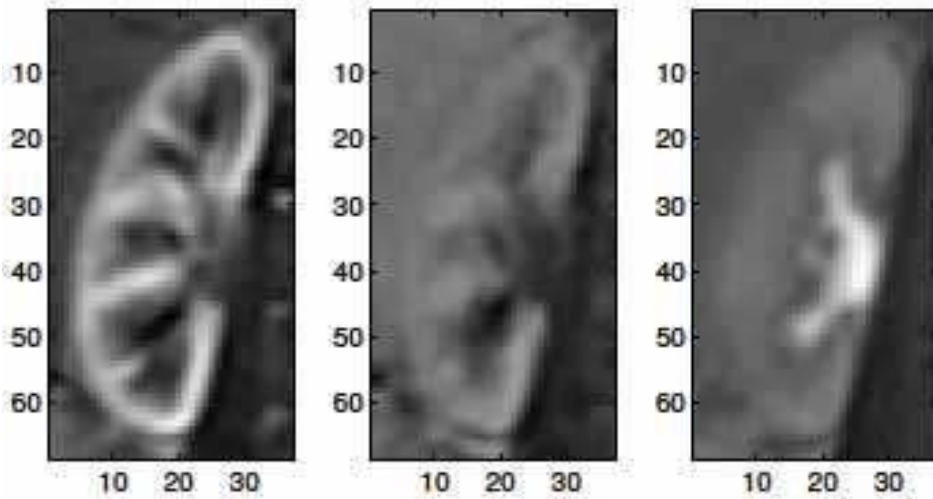
Fig. 1. Examples of frames from a DCE-MRI sequence during arterial peak (left), filtration (middle) and late phase (right)

The aim is to find a set $\{w_j\}_{1 \leq j \leq K} \subset X$ of prototypes (or nodes) that maps the distribution with a given distortion. Let be $w(\xi) = \arg\min_{w_j} \|\xi - w_j\|^2$. The Growing Neural Gas with targeting (GNG-T) (Frezza-Buet, 2008), which is a variant of the classical Growing Neural Gas algorithm (Fritzke, 1995), minimizes a cost function that tends towards the distortion:

$$E = \int_X \|w((\xi) - \xi\|^2 p(\xi)d\xi = \sum_{j=1}^{K} E_j \qquad (1)$$

where

$$E_j = \int_{V_j} \|w_j - \xi\|^2 p(\xi)d\xi \text{ and } V_j = \{\xi \in X : w(\xi) = w_j\} \qquad (2)$$

$V_j$ is the so-called Voronoï cell of $w_j$ and consists of all points of $X$ that are closer to $w_j$ than to any other $w_i$. The set of $\{V_j\}_{1 \leq j \leq K}$ is a partition of $X$.

More precisely, GNG-T algorithm builds iteratively a network consisting in both:
- a set of prototypes,
- a graph structure preserving the topology of the underlying probability distribution.

This graph is made up of a set of connections between nodes defining a topological neighbourhood relation in the parameter space. It approximates the induced Delaunay triangulation of the set $\{w_j\}_{1 \leq j \leq K}$ on the manifold $X$ (Martinetz et al., 1993). Edges are drawn up according to a competitive Hebbian learning rule: the basic principle is, for each input $\xi_i$, to connect the two best matching prototypes. Two prototypes that are directly

linked in the final graph should thus have similar temporal behaviour. Both the winner, i.e. the closest prototype of the current data point, and all its topological neighbours are adjusted after each iteration. Influence of initialization is thus reduced for GNG-T compared to on-line K-means for instance.

The number $K$ of prototypes is iteratively determined to reach a given average node distortion $T$. While a prior lattice has to be chosen for other algorithms like self-organising map (Kohonen, 2001), no topological knowledge is required here: the graph adapts automatically to any distribution structure during the building process.

GNG-T is an iterative algorithm that processes successive epochs. During each epoch, $N$ samples $\left(\xi_j\right)_{1 \leq i \leq N}$ are presented as GNG-T inputs. An accumulation variable $e_j$ is associated with each node $w_j$: it is initialized to zero at the beginning of the epoch and is updated every time $w_j$ actually wins by adding the error $\left\|\xi_i - w_j\right\|^2$. When the cost function defined in equation (1) is minimal, all the $E_j$ reach the same value, denoted $T'$. For a given epoch, $E_j$ can be estimated by:

$$E_j \approx \frac{e_j}{N} \tag{3}$$

$T'$ helps to adapt the number of nodes at the end of each epoch. It is then compared to the desired target $T$. If $T' > T$, vector quantization is not accurate enough: a new node is thus added between the node $w_{j_0}$ with the strongest accumulated error $e_{j_0}$ and its topological neighbour $w_{j_1}$ with the strongest error $e_{j_1}$, and the edges are adapted accordingly. If $T' < T$, the node with the weakest accumulated error is eliminated to reduce accuracy. All implementation details can be found in (Frezza-Buet, 2008).

Let us note that the aim of the algorithm is not to classify pixels but to perform vector quantization. For this reason it tends to give a fairly large $K$ value. A given class is actually represented by a subset of connected nodes, and all points that belong to the union of their associated Voronoï cells are attributed to this class. As an example, the quantization results and the boundaries of the clusters for a two-dimensional Gaussian mixture distribution are given in figure 2 (notice that our problem is $N_T$-dimensional). Nevertheless, for real cases, a single connected network is obtained most of the time because of noise and because the distributions are not straightforwardly separable. So an additional merging step is mandatory in order to break non significant edges and then obtain the final segmentation in three anatomical compartments.
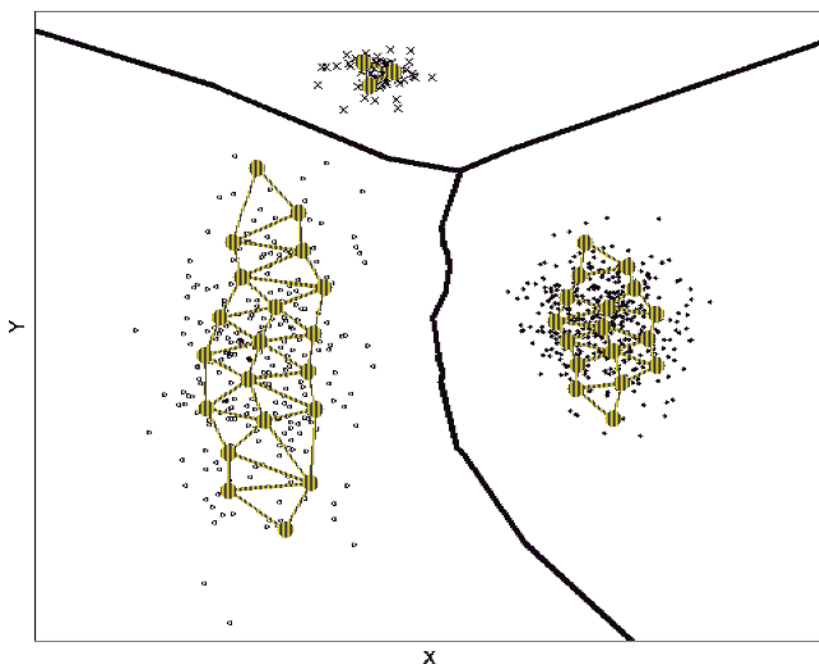
Fig. 2. Results of a vector quantization by GNG-T procedure with final partition (large solid lines): small dots represent samples of the distribution, large dots are the resulting nodes linked with edges.


## 2.2 Formation of the three final compartments for real data

Each node has then to be assigned to one of the three anatomical compartments. Typical time-intensity curves with the main perfusion phases (baseline, arterial peak, filtration, equilibrium and late phase) are shown in figure 3.

Nevertheless, for a given kidney, noticeable differences can be observed inside each compartment (see figure 4). The Euclidean distance between curves is therefore not a criterion significant and robust enough to aggregate nodes. Indeed the distance between two prototypes of two distinct ROIs may often be smaller than disparity within a single compartment. This is true even if distance is evaluated only for points of filtration, during which contrast evolutions should be the most different. It is why some physiology related characteristics of the contrast evolution have to be used to get the final compartments.

We proceed as follows:

- First, as cavities should be the brighter structure in the late phase (see figure 3) due physiological reasons, nodes whose average intensity during this stage is greater than a given threshold $t_1$ and that are directly connected to each other in the GNG graph are considered as cavities.
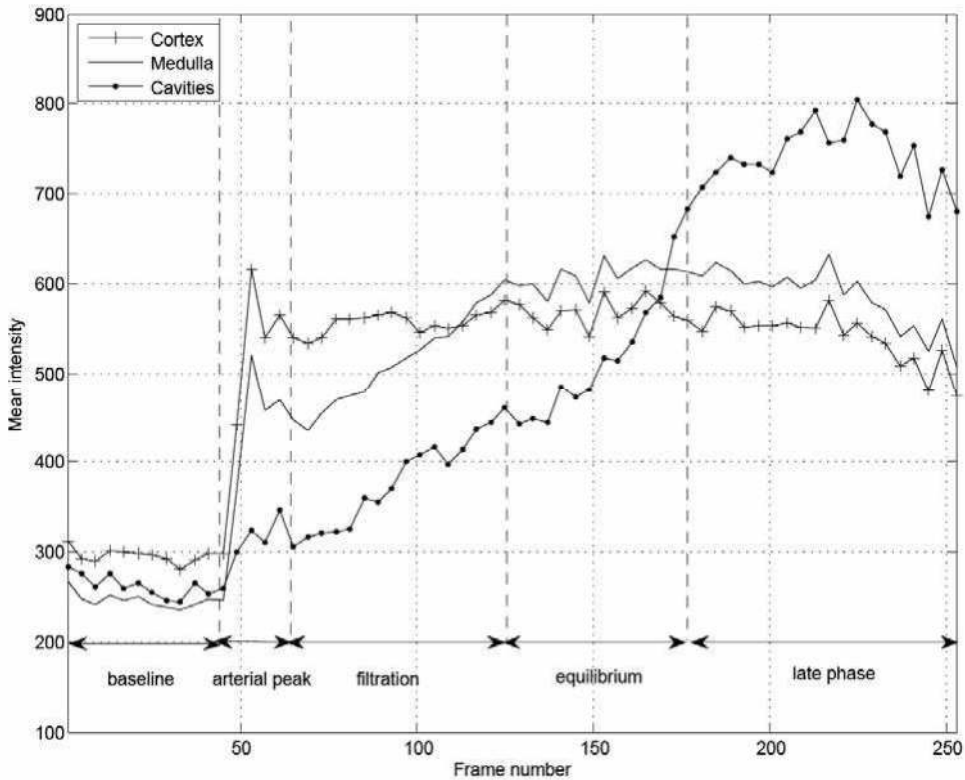
Fig. 3. Typical time-intensity curves for cortex, medulla and cavities

- In a second step, filtration phase is used to separate cortex and medulla. Filtration rate depends on the tissue nature. So the slope of time-intensity curves during filtration (see figure 3) is evaluated using standard linear regression for all remaining prototypes: a node is attributed to the cortex if the corresponding slope is less than a given threshold $t_2$, else it is assigned to the medulla.

The two thresholds $t_1$ and $t_2$ are initialized so that cortex represents approximately 50% and cavities about 20% of kidney area and are adjusted by an observer. This is the only manual intervention of the whole operation. As the algorithm is very fast, the tuning step can be done in real time. Let us stress that the second criterion would not be sufficient to distinguish cavities from cortex and medulla because of a theoretically unexpected but fairly high arterial peak that can be observed in figure 4(c): this peak is induced by the great vascularization of the whole kidney and may appear in all ROIs. Furthermore the use of topological edges for cavities determination avoids classifying in this compartment some nodes that have a similar contrast in late phase but whose behaviour differs sufficiently in other filtration phases.
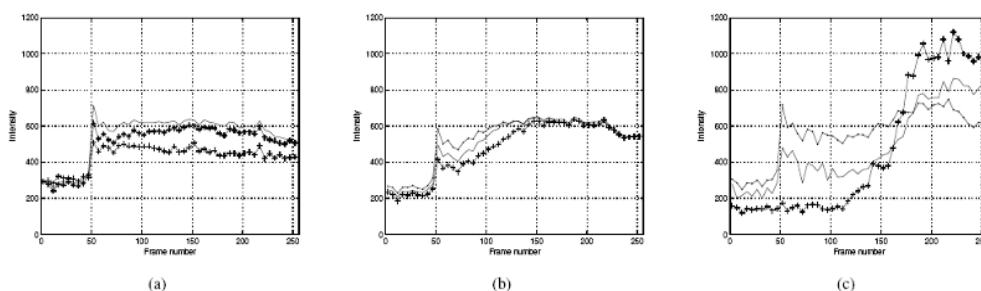
Fig. 4. Some examples of time-intensity curves for prototypes attributed to cortex (a), medulla (b) and cavities (c) of a given kidney

## 3. Experiment

### 3.1 Materials

Eight two-dimensional low resolution DCE-MRI sequences of normal kidney perfusion with 256 images were used (acquisition duration: about 12 minutes, temporal resolution: about 3 s). The examinations were performed on a whole-body 1.5T MR-scanner (General Electric Healthcare). A 3D ultrafast gradient echo LAVA sequence was used with the following parameters: 15° flip angle, TR/TE 2.3 ms/1.1 ms. The slice that contained the largest surface of renal tissue was then selected. The initial matrix size was 256×256 with pixel size between 1.172 mm and 1.875 mm (slice thickness: 10 mm). A rectangular area containing kidney was delineated (size between 47×35 and 84×59). In-plane movements due to respiration were corrected by a rigid registration algorithm including translations and rotation. Because of rapid and high contrast changes during perfusion mutual information was chosen as a similarity criterion (Pluim et al., 2003). Anyway through-plane motions remained and frames were highly noisy. An example of frames for three different perfusion phases is shown in figure 1.

### 3.2 Manual segmentations by radiologists

The different sequences were presented to two experienced radiologists (OP1 and OP2) after automatic registration. They had to delineate three ROIs, namely the cortex, the medulla and the pelvo-caliceal cavities as well as a global kidney mask. To do so, the following procedure was set up:

1. visualization of the complete sequence,
2. selection of a late phase frame were cavities contrast is maximum and manual segmentation of the cavities,
3. identification of the frame corresponding to the cortical enhancement peak and manual segmentation of the cortex,
4. segmentation of medulla by difference with cortex and cavities already segmented.

A global mask was then extracted as the common area of the two manual segmentations, including the three ROIs delineated by the two radiologists. This mask was subsequently used for functional segmentation (only pixels inside this mask were used by the GNG-T algorithm). Two examples of manual segmentations can be seen in figure 5.

### 3.3 Discrepancy criteria for segmentation comparison

For each of the eight cases a manual segmentation is considered as a reference. The functional segmentation obtained thanks to the proposed method or another manual one will be both compared to this reference.

Every segmentation can be considered as a binary map, with label 1 inside the ROI and label~0 outside. Let be R the reference segmentation and T the tested one. Four types of pixels can then be defined, according to their labels in R and T:

| Pixel type | Label in R | Label in T |
|------------|------------|------------|
| True Positive (TP) | 1 | 1 |
| False Negative (FN) | 1 | 0 |
| False Positive (FP) | 0 | 1 |
| True Negative (TN) | 0 | 0 |

Four discrepancy measures between R and T are evaluated for each ROI:

- percentage overlap $PO = 100 \times TP/(TP + FN)$, i.e. percentage of pixels of the reference ROI that are in the test ROI too,

- percentage extra $PE = 100 \times FP/(TP + FN)$, i.e. the number of pixels that are in the test ROI while they are out of reference ROI, divided by the number of pixels in the reference ROI. Perfect segmentation would give $PO = 100\%$ and $PE = 0\%$. High values for both $PO$ and $PE$ for a given segmentation tend to point out some oversegmentation of the corresponding compartment. A high $PE$ associated to a weak $PO$ may indicate that the ROI is globally wrong positioned.

- similarity index $SI = 2 \times TP/(TP + FN + FP)$. $SI$ is sensitive to both differences in size and location (Zijdenbos et al., 1994). For instance two equally sized ROIs that share half of their pixels would yield $SI = 1/2$. A ROI covering another that is twice as little would give $SI = 2/3$. For a perfect segmentation the $SI$ value would be 1.

- mean distance $MD$ (in pixel) between contours of test and reference segmentation: $MD$ is the average distance between every pixel of the contour in the test segmentation and the closest pixel of the reference contour.

$SI$ is the only selected criterion that is independent of the chosen reference, however its values appear twice in the tables in order to facilitate comparisons.

## 4. Results

Examples of two manual segmentations and of a functional semi-automated one can be seen in figure 5. For this case, size of ROIs varies between 532 and 700 pixels for cortex, 375 and 559 for medulla, 161 and 217 for cavities. The delineated contours are superimposed on MR images of the renal pixels (region out of the global kidney mask is black). Frames correspond to perfusion phases during which each compartment is visible at best:

- arterial peak for cortex and medulla
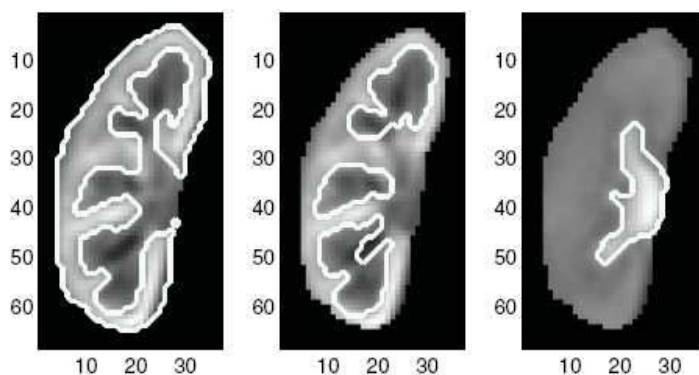- late phase for cavities.
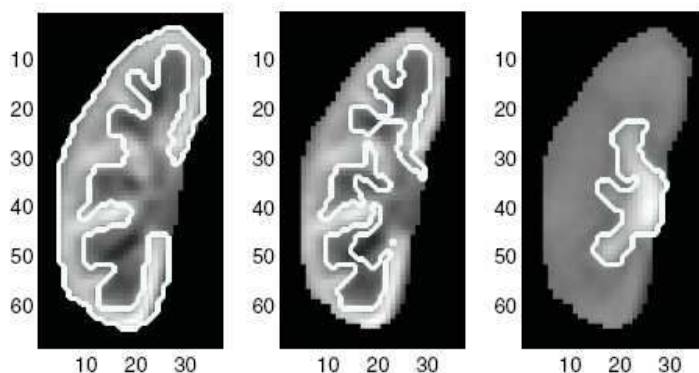
(a) Anatomical manual segmentation (OP1)
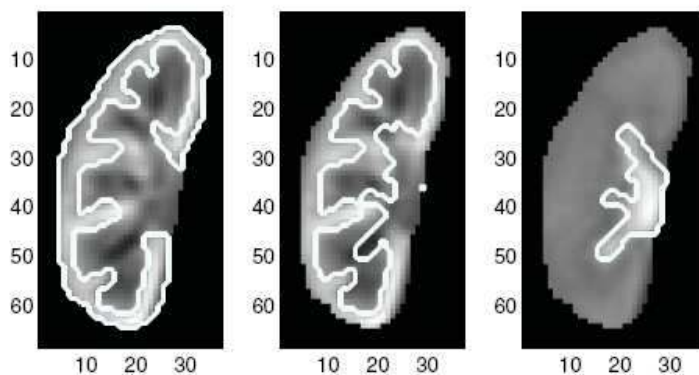


(b) Anatomical manual segmentation (OP2)



(c) Functional semi-automated segmentation

Fig.5. Example of cortex (left), medulla (middle) and cavities (right) segmentations

For almost all the tested kidneys, a very good visual qualitative consistency between these frames and functional segmentation is obtained.

For quantitative comparisons the manual segmentation OP1 is first considered as the reference. Table 1 Part 1 shows for each type of ROI, means over the eight cases of discrepancy measures between:

- the semi-automated segmentation (GNG-T) and OP1,
- the second manual segmentation (OP2) and OP1.

In table 1 Part 2, on the other hand, the reference is OP2. The percentage of well classified pixels for a given compartment is the sum of TP pixels over the eight cases divided by the total number of pixels for this type of ROI. For global kidney it is the sum of TP pixels for all ROIs over the eight cases divided by the total number of pixels of all kidney global masks. Results for small kidneys have less influence on this percentage than on mean overlap.

| Segmentation by | OP2 | GNG-T |
|---|---|---|
| Well classified pixels (%) | 69.8 | 83.7 |
| Overlap (%) | 71.8 | 83.2 |
| Extra pixels(%) | 9.2 | 21.9 |
| Similarity index | 0.79 | 0.81 |
| Mean distance to reference contour | 0.6 | 0.8 |

(a) Cortex

| Segmentation by | OP2 | GNG-T |
|---|---|---|
| Well classified pixels (%) | 84.8 | 73.0 |
| Overlap (%) | 84.0 | 73.0 |
| Extra pixels(%) | 56.6 | 33.7 |
| Similarity index | 0.70 | 0.71 |
| Mean distance to reference contour | 1.0 | 0.8 |

(b) Medulla

| Segmentation by | OP2 | GNG-T |
|---|---|---|
| Well classified pixels (%) | 74.9 | 68.7 |
| Overlap (%) | 73.9 | 69.8 |
| Extra pixels(%) | 16.1 | 11.1 |
| Similarity index | 0.77 | 0.77 |
| Mean distance to reference contour | 0.8 | 0.7 |

(c) Cavities

| Segmentation by | OP2 | GNG-T |
|---|---|---|
| Well classified pixels (%) | 74.9 | 77.6 |

(d) Global kidney

**Part 1**

| Segmentation by | OP1 | GNG-T |
|---|---|---|
| Well classified pixels (%) | 89.7 | 85.8 |
| Overlap (%) | 89.0 | 85.7 |
| Extra pixels(%) | 36.1 | 34.8 |
| Similarity index | 0.79 | 0.78 |
| Mean distance to reference contour | 0.7 | 0.9 |

(a) Cortex

| Segmentation by | OP1 | GNG-T |
|---|---|---|
| Well classified pixels (%) | 60.3 | 69.7 |
| Overlap (%) | 60.5 | 69.9 |
| Extra pixels(%) | 11.8 | 16.3 |
| Similarity index | 0.70 | 0.75 |
| Mean distance to reference contour | 1.0 | 0.9 |

(b) Medulla

| Segmentation by | OP1 | GNG-T |
|---|---|---|
| Well classified pixels (%) | 81.8 | 74.9 |
| Overlap (%) | 82.2 | 76.4 |
| Extra pixels(%) | 32.4 | 12.6 |
| Similarity index | 0.77 | 0.80 |
| Mean distance to reference contour | 0.9 | 0.5 |

(c) Cavities

| Segmentation by | OP1 | GNG-T |
|---|---|---|
| Well classified pixels (%) | 74.9 | 76.7 |

(d) Global kidney

**Part 2**

Table 1. Discrepancy measures for segmentations of the three ROIs when OP1 (Part 1) or OP2 (Part 2) are considered as a reference.

Similarity measures between functional segmentation and any manual segmentation are very similar to those computed between the two manual ones. A better score for overlap is always compensated by an increase of extra pixels. The percentage of globally well classified pixels is even higher for the proposed method, and the similarity index and the mean distance between contours are most of the time better. This was not the case for k-means clustering of the time-intensity curves, where scores were lower for functional segmentation (Chevaillier et al., 2008a): for instance an increase of 3 to 6% in the percentage of globally well classified pixels can be noted for the new method. Furthermore results do not depend significantly on the type of ROI. The quality of functional segmentation does not change

with the region size: cavities that are much smaller than the two other ROIs are recovered as correctly as those. Moreover this technique is fast and user-friendly. The size of the prototype set stemming from GNG-T varies between 10 and 30 nodes: it depends essentially on temporal evolution complexity induced in particular by vascularization artefacts and highly noisy acquisition but little on kidney size. Nevertheless operator has only to adjust two thresholds: the first allows extracting cavities by adding or taking off the most relevant nodes, whereas the second is used in the same way to set relative areas of cortex and medulla. The splitting step with GNG-T allows to consider first the global time-intensity evolution and to reduce noise effect; the threshold adjustment is then easier because at each tuning level a relatively numerous set of pixels with homogenous temporal evolution is added.

## 5. Conclusion and perspectives

A semi-automated method for functional segmentation of internal kidney structures using DCE-MRI sequences was tested and compared with manual segmentations by radiologists. Good qualitative consistency between the two types of segmentation is observed. Similarity measures between a manual segmentation and a functional one are comparable and often better than the same criteria evaluated between two manual segmentations. Results are better than those obtained with the k-means algorithm applied on the same data: for instance the percentage of well classified pixels is 3 to 6% higher. Let us note that the derived time-intensity curves of each compartment are almost identical for functional or manual segmentation. Thus the method is suitable for renal segmentation from DCE-MRI. Moreover this technique is user friendly because the only manual intervention during the whole segmentation process consists in the coarse real-time tuning of two independent thresholds. It offers more reproducibility and is also greatly faster than manual segmentation: the latter requires 12 to 15 minutes for one sequence, versus about 30 seconds for the former, including threshold adjustment. To validate the method further tests will be performed on a larger database including both healthy and pathological kidneys. In the latter case, an adaptation of the physiological criteria previously used to obtain the final compartments can be needed because new temporal behaviours may appear.

## 6. References

Chevaillier, B. ; Ponvianne, Y. ; Collette, J.L. ; Mandry, D. ; Claudon, M. & Pietquin, O. (2008a). Functional semi-automated segmentation of renal DCE-MRI sequences, *Proceedings of the IEEE International Conference on Acoustics, Speech and Signal Processing (ICASSP 2008)*, pp. 525-528, ISBN 1-4244-1484-9, Las Vegas (NV, USA), March 2008..

Chevaillier, B. ; Ponvianne, Y. ; Collette, J.L. ; Mandry, D. ; Claudon, M. & Pietquin, O. (2008b). Functional semi-automated segmentation of renal DCE-MRI sequences using a Growing Neural Gas algorithm, *Proceedings of the 16th European Signal Processing Conference (EUSIPCO 08)*, EURASIP, Lausanne (Switzerland), August 2008.

Coulam, C.H.; Bouley, D.M. & Sommer, F.G. (2002). Measurement of renal volumes with contrast-enhanced MRI. *Journal Of Magnetic Resonance Imaging,* Vol. 15, No. 2, February 2002, pp. 174-179, ISSN 1053-1807

Frezza-Buet, H. (2008). Following non-stationary distributions by controlling the vector quantization accuracy of a growing neural gas network. *Neurocomputing,* Vol. 71, No7-9., March 2008, pp. 1191-1202, ISSN 0925-2312

Fritzke, B. (1995). A growing neural gas network learns topologies, *Advances in Neural Information Processing Systems, Proceedings of 1995 Conference*, pp. 625-632, ISBN 0-262-20107-0, Denver CO, November 1995, D. S. Touretzky, M. C. Mozer, M. E. Hasselmo, eds. MIT Press, Cambridge

Grenier, P.; Basseau, F. ; Ries, M. ; Tyndal, B. ; Jones, R. & Moonen, C. (2003). Functional MRI of the kidney, *Abdominal Imaging,* Vol. 28, No.2, March 2003, pp. 164-175, ISSN 0942-8925

Kohonen, T. (2001). *Self-organizing maps,* Springer, ISBN 9783540679219, New York

Lv, D.; Zhuang, J.; Chen, H.; Wang, J.; Xu, Y.; Yang, X.; Zhang, J.; Wang, X. & Fang, J. (2008). Dynamic contrast-enhanced magnetic resonance images of the kidney. *IEEE Engineering in Medicine and Biology Magazine,* Vol. 27, No. 5, September 2008, pp. 36-41, ISSN 0739-5175

Martinetz, T.; Berkovich, S. & Schulten, K. (1993). Neural-gas Network for Vector Quantization and its Application to Time-Series Prediction. *IEEE-Transactions on Neural Networks,* Vol. 4, No. 4, July 1993, pp. 558-569, ISSN 1045-9227

Michoux, N.; Vallee, J.P. ; Pechere-Bertschi, A. ; Mintet,X. ; Buehler, L. & Beers, B. (2006). Functional MRI of the kidney, *Abdominal Imaging,* Vol. 28, No.2, march 2003, pp. 164-175, ISSN: 0942-8925

Pluim, J.P.W.; Maintz, J.B.A. & Viergever, M.A. (2003). Mutual-information-based registration of medical images: a survey. *IEEE Trans. Med. Imaging,* Vol. 22, No. 8, (2003) pp. 986-1004, ISSN 0278-0062

Song, T.; Lee, V.S.; Rusinek, H.; Sajous, J.B. & Laine, A.F. (2005). Registration and Segmentation of Dynamic Three-dimensional MR Renography Based on Fourier Representations and K-Means Clustering, *Proceedings of ISMRM 13th Scientific Meeting*, ISSN 1545-4428, Miami Beach (FL, USA), May 2005.

Sun, Y.; Moura, J.M.F. & Chien Ho. (2004). Subpixel registration in renal perfusion MR image sequence, *2nd IEEE International Symposium on Biomedical Imaging: Macro to Nano (IEEE Cat No. 04EX821)*, pp. 700-3, ISBN 0-7803-8388-5, Arlington (VA, USA), April 2004

Zijdenbos, A.P.; Dawant, B.M.; Margolin, R.A. & Palmer, A.C. (1994). Morphometric analysis of white matter lesions in MR images: method and validation. *IEEE Trans. Med. Imaging,* Vol. 13, No. 4, December 1994, pp. 716-24, ISSN 0278-0062

Zoellner, F.G.; Sance, R.; Anderlik, A.; Roervik, J.; Kocinski, M. & Lundervold, A. (2006). Towards quantification of kidney function by clustering volumetric MRI perfusion time series. *Magnetic Resonance Materials in Physics, Biology and Medicine,* Vol. 19, September 2006, pp. 103-104, ISSN 0968-5243
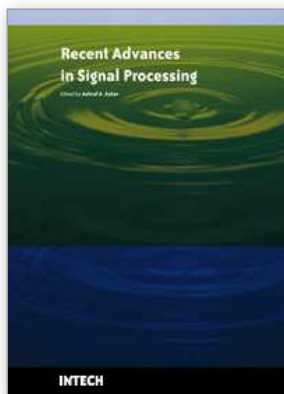
**Recent Advances in Signal Processing**

Edited by Ashraf A Zaher

The signal processing task is a very critical issue in the majority of new technological inventions and challenges in a variety of applications in both science and engineering fields. Classical signal processing techniques have largely worked with mathematical models that are linear, local, stationary, and Gaussian. They have always favored closed-form tractability over real-world accuracy. These constraints were imposed by the lack of powerful computing tools. During the last few decades, signal processing theories, developments, and applications have matured rapidly and now include tools from many areas of mathematics, computer science, physics, and engineering. This book is targeted primarily toward both students and researchers who want to be exposed to a wide variety of signal processing techniques and algorithms. It includes 27 chapters that can be categorized into five different areas depending on the application at hand. These five categories are ordered to address image processing, speech processing, communication systems, time-series analysis, and educational packages respectively. The book has the advantage of providing a collection of applications that are completely independent and self-contained; thus, the interested reader can choose any chapter and skip to another without losing continuity.

**How to reference**

In order to correctly reference this scholarly work, feel free to copy and paste the following:

# INTECH
open science | open minds